RESEARCH ARTICLE

Check for updates

A novel hierarchical precursor of densely integrated hydroxide nanoflakes on oxide microspheres toward high-performance layered Ni-rich cathode for lithium ion batteries†

Yan Li,[a] Xinhai Li, [iD] [a] Zhixing Wang, [iD] [a] Huajun Guo, [iD] [a] Tao Li,[a] Kui Meng[a] and Jiexi Wang [iD] *[ab]

Herein, a novel hierarchical precursor of $Ni_{0.8}Co_{0.1}Mn_{0.1}O_x@Ni_{0.8}Co_{0.1}Mn_{0.1}(OH)_2$ is proposed for the first time, which was synthesized by densely integrating co-precipitated $Ni_{0.8}Co_{0.1}Mn_{0.1}(OH)_2$ nanoflakes onto spray-pyrolyzed $Ni_{0.8}Co_{0.1}Mn_{0.1}O_x$ microspheres. The co-precipitated hydroxide layer can prevent the $Ni_{0.8}Co_{0.1}Mn_{0.1}O_x$ microspheres from fragmenting during the sintering process, thus yielding uniform $LiNi_{0.8}Co_{0.1}Mn_{0.1}O_2$ spheres with a hollow interior morphology. Strikingly, the obtained spherical $LiNi_{0.8}Co_{0.1}Mn_{0.1}O_2$ cathode exhibits improved tap density and initial coulombic efficiency, as well as excellent cycling stability and superior rate capability. Discharge capacities of 169 mA h g^{-1} after 300 cycles at 1C (180 mA g^{-1}) of between 2.8 and 4.3 V are consistently obtained, corresponding to 90.5% capacity retention. Significantly, it is strongly envisioned that this novel hierarchical structure design concept holds great promise for the architectural construction of other energy storage materials.

1. Introduction

Green-energy technology has witnessed rapid development due to the increasingly serious energy crisis and environmental contamination.[1–6] Lithium ion batteries (LIBs) are considered to be one of the most promising power sources for electric vehicles and stationary energy storage.[7–14] However, technical solutions to further increase the energy density and reduce the cost of LIBs are essential.[15–24] Because of their high specific capacity and relatively low cost, layered Ni-rich cathode materials have been intensively investigated.[25–27] As mineral resources continue to be depleted, the utilization of lean ore and resource reclamation are inevitable options for guaranteeing resource sustainability. Hydrochloric acid leaching is an efficient method used for the extraction of Ni and Co from low-grade laterite ores and spent LIBs. However, it is urgently necessary to develop an approach to efficiently utilization of the obtained transition metal chlorides.

Spray pyrolysis is an effective, easily controlled and versatile method for material preparation.[28–31] Spray pyrolysis has been developed for the production of layered cathode materials ($LiNi_{1/3}Co_{1/3}Mn_{1/3}O_2$, $Li_{1.2}Mn_{0.54}Ni_{0.13}Co_{0.13}O_2$),[32,33] olivine phosphates ($LiMPO_4$; M = Fe, Co, Ni and Mn)[34–36] and spinel oxides (LiM_2O_4, M = Mn, Ni and Co),[37,38] and these materials have shown excellent electrochemical performance. Very recently, we reported a comprehensive study of $LiNi_{0.8}Co_{0.1}Mn_{0.1}O_2$ synthesized *via* spray pyrolysis. The obtained material exhibited extraordinary cycling stability, revealing the distinct advantages of spray pyrolysis in preparing Ni-rich layered cathodes.[39] However, this material showed a low tap density due to the irregular submicron size and poor powder flowability. Many approaches have been developed to improve the tap density of materials prepared by spray pyrolysis. Miklos Lengyel *et al.* introduced an approach called "Flame Assisted Spray Technology-Slurry Spray Pyrolysis" to avoid hollow sphere formation, in which the tap density of layered cathode increased from ∼0.5 g cm^{-3} to 1.05 g cm^{-3}.[40] S. H. Ju *et al.* prepared spherical $LiNi_{0.8}Co_{0.15}Al_{0.05}O_2$ and $LiNi_{0.8}Co_{0.15}Mn_{0.05}O_2$ cathode powders with filled morphology *via* spray pyrolysis from a spray solution containing organic additives and a drying control chemical additive.[41,42] These approaches can improve the tap density to a certain degree, but are still not sufficient for commercial utilization.

Herein, to improve the tap density of Ni-rich materials prepared by spray pyrolysis, a novel hierarchical architecture is introduced *via* densely integrating co-precipitated hydroxide

[a] School of Metallurgy and Environment, Central South University, Changsha 410083, P. R. China. E-mail: wangjiexikeen@csu.edu.cn

[b] State Key Laboratory of Powder Metallurgy, Central South University, Changsha 410083, P. R. China

† Electronic supplementary information (ESI) available: Chemical composition and particle size distribution of the precursor and cathode samples, SEM and XRD of the $Ni_{0.8}Co_{0.1}Mn_{0.1}O_x$ and $Ni_{0.8}Co_{0.1}Mn_{0.1}(OH)_2$ precursors, the cycle performance of the $LiNi_{0.8}Co_{0.1}Mn_{0.1}O_2$ cathodes prepared from the $Ni_{0.8}Co_{0.1}Mn_{0.1}O_x$ and $Ni_{0.8}Co_{0.1}Mn_{0.1}(OH)_2$ precursors. See DOI: 10.1039/c8qm00326b

nanoflakes onto spray pyrolyzed $Ni_{0.8}Co_{0.1}Mn_{0.1}O_x$ microspheres. As expected, the co-precipitated hydroxide layer could prevent the $Ni_{0.8}Co_{0.1}Mn_{0.1}O_x$ microspheres from fragmenting during the sintering process, and thus yield uniform $LiNi_{0.8}Co_{0.1}Mn_{0.1}O_2$ spheres. The obtained $LiNi_{0.8}Co_{0.1}Mn_{0.1}O_2$ spheres with thick shells show an obviously increased tap density and inherit the excellent electrochemical performance of $LiNi_{0.8}Co_{0.1}Mn_{0.1}O_2$ prepared from spray pyrolyzed $Ni_{0.8}Co_{0.1}Mn_{0.1}O_x$ microspheres.

2. Experimental

2.1. Materials preparation

A schematic of the preparation process for the $LiNi_{0.8}Co_{0.1}Mn_{0.1}O_2$ spheres is shown in Scheme 1. The $Ni_{0.8}Co_{0.1}Mn_{0.1}O_x$ microspheres were synthesized using the spray pyrolysis method. The precursor solution was prepared by dissolving $NiCl_2 \cdot 6H_2O$, $CoCl_2 \cdot 6H_2O$ and $MnCl_2 \cdot 4H_2O$ in distilled water at the molar ratio of 8 : 1 : 1. The precursor solution was aerosolized using a 1.75 MHz ultrasonic nebulizer. The droplet stream was carried into a 3-zone vertical furnace reactor by O_2 with a flow rate of 5 L min^{-1}. The spray pyrolysis temperature was maintained at 750 °C. The resulting $Ni_{0.8}Co_{0.1}Mn_{0.1}O_x$ powder was collected at the reactor exit.[39] The spray pyrolyzed $Ni_{0.8}Co_{0.1}Mn_{0.1}O_x$ microspheres and 200 mL NH_4OH solution (2 mol L^{-1}) were added into a reactor of 1 L capacity. Then, an aqueous solution consisting of $NiCl_2$, $CoCl_2$ and $MnCl_2$ with a concentration of 0.5 mol L^{-1} was continuously fed into the reactor. At the same time, a NH_4OH solution as the chelating agent (2 mol L^{-1}) and NaOH solution (1.0 mol L^{-1}) were also separately pumped into the reactor. The temperature (55 °C), stirring speed (400 rpm), and pH value (pH = 11.5) were carefully controlled during the precipitation reaction in the reactor. After 2 hours, the precursor was filtered, thoroughly washed with distilled water, and dried overnight at 80 °C. $LiNi_{0.8}Co_{0.1}Mn_{0.1}O_2$ was prepared by thoroughly

mixing the hierarchical $Ni_{0.8}Co_{0.1}Mn_{0.1}(OH)_2@Ni_{0.8}Co_{0.1}Mn_{0.1}O_x$ precursor powder with Li_2CO_3, followed by calcining at 780 °C for 15 h in flowing oxygen.

2.2. Material characterization

The as-prepared powders were characterized using X-ray diffraction (XRD, Rint-2000, Rigaku). Particle morphology was examined with scanning electron microscopy (SEM, Sirion 200) and transmission electron microscopy (TEM, Tecnai G12, 200 kV). Inductively Coupled Plasma-Optical Emission Spectrometry (ICP, IRIS intrepid XSP) was used to determine the composition of the precursor powders and the annealed powders. The particle size distributions of the precursor and cathode materials were characterized using a laser particle size analyzer (Malvern, Mastersizer 2000). The tap density of the cathode sample was measured via a FZS4-4B Tap Density Apparatus. The mass of the cathode sample was measured using an electronic balance. The sample was placed into a measuring cylinder, oscillated 3000 times perpendicularly by the apparatus. Then the volume readings were recorded. The tap density was calculated as mass divided by volume.

2.3. Electrochemical measurements

Electrochemical performance was evaluated in CR2025-type coin cells assembled in an argon-filled glove box with both the moisture and oxygen content below 0.1 ppm. Cathode film fabrication was performed according to the procedure reported earlier.[43] The working electrode comprised 80 wt% $LiNi_{0.8}Co_{0.1}Mn_{0.1}O_2$, 10 wt% ketjin black and 10 wt% polyvinylidene fluoride (PVdF). The average loading of electroactive $LiNi_{0.8}Co_{0.1}Mn_{0.1}O_2$ was ~ 1.2 mg per disk (12 mm in diameter). The electrolyte solution was 1 M $LiPF_6$ in an ethylene carbonate/ethyl methyl carbonate/dimethyl carbonate solution (EC : EMC : DMC = 1 : 1 : 1, v/v/v). Cyclic voltammetry (CV) and electrochemical impedance spectroscopy (EIS) were performed on a CHI 660A electrochemical workstation. Charge/discharge tests were performed on a NEWARE BTS-51 battery tester.

3. Results and discussion

The XRD patterns of the precursor (Fig. 1) can be attributed to a mixed phase of NiO, $MnCo_2O_4$ and β-$Ni(OH)_2$, demonstrating that the precursor is comprised of the spray pyrolyzed oxides and co-precipitation derived hydroxides. The Rietveld refinement results of the XRD patterns of $LiNi_{0.8}Co_{0.1}Mn_{0.1}O_2$ (Fig. 2) show that the as-prepared sample adopts a typical layered hexagonal α-$NaFeO_2$ structure. It was found that the ratio of $I_{(003)}/I_{(104)}$ is 1.68 and the amount of Ni^{2+} in the Li sites is 3.76%, indicating a low degree of cation mixing. The clear split of the (006)/(102) and (108)/(110) peaks suggest that the sample has a high degree of ordered hexagonal structure. A superior layered structure and low degree of cation mixing are conducive to improving the electrochemical performance of a cathode. The compositions of the precursor and the as-prepared cathode material were measured by ICP (Table S1, ESI†). The results
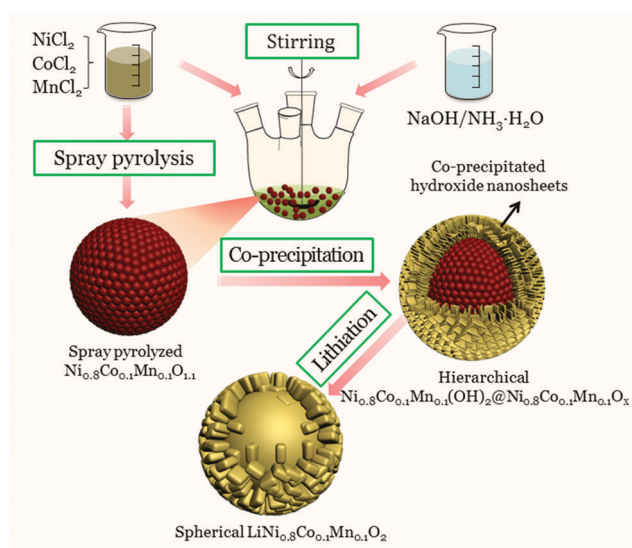
Scheme 1 Schematic diagram of the synthesis process for the $LiNi_{0.8}Co_{0.1}Mn_{0.1}O_2$ microspheres.

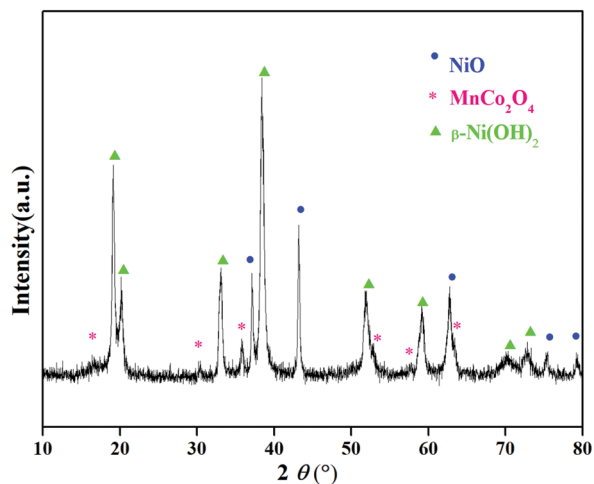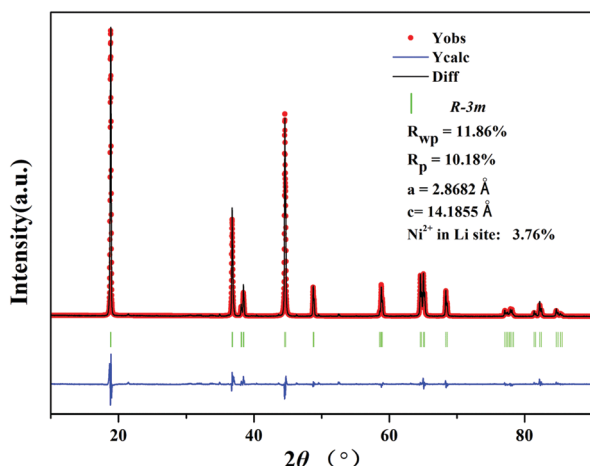Fig. 1 XRD patterns of the $Ni_{0.8}Co_{0.1}Mn_{0.1}(OH)_2@Ni_{0.8}Co_{0.1}Mn_{0.1}O_x$ precursor.

Fig. 2 Rietveld refinement profile of the XRD data of the $LiNi_{0.8}Co_{0.1}Mn_{0.1}O_2$ cathode prepared from $Ni_{0.8}Co_{0.1}Mn_{0.1}(OH)_2@Ni_{0.8}Co_{0.1}Mn_{0.1}O_x$.
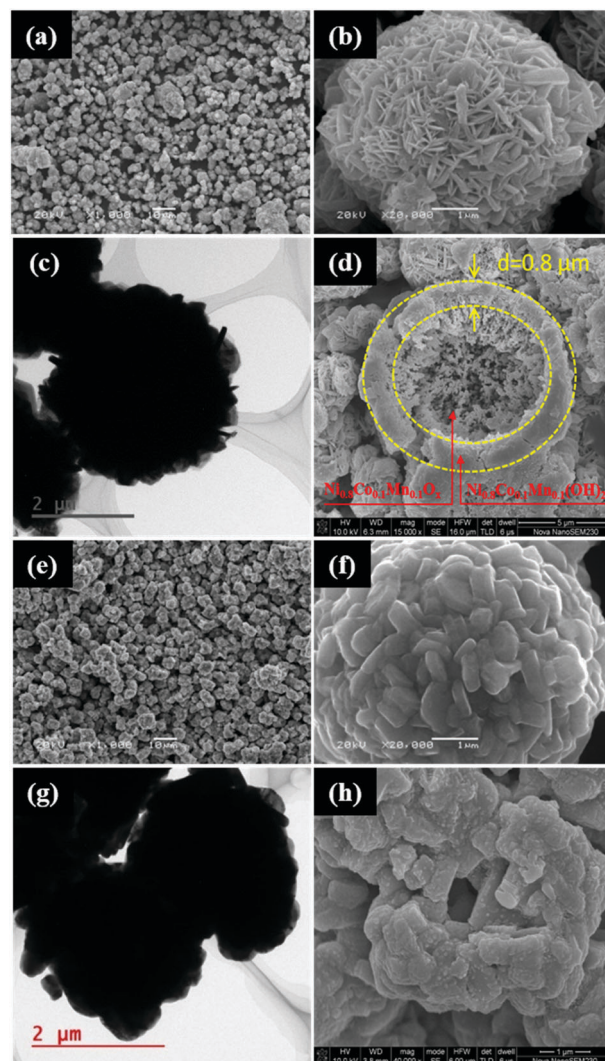

Fig. 3 (a) Low-magnification SEM, (b) high-magnification SEM, (c) TEM and (d) cross-sectional SEM images of the holistic $Ni_{0.8}Co_{0.1}Mn_{0.1}(OH)_2@Ni_{0.8}Co_{0.1}Mn_{0.1}O_x$ precursor. (e) Low-magnification SEM, (f) high-magnification SEM, (g) TEM and (h) cross-sectional SEM images of the $LiNi_{0.8}Co_{0.1}Mn_{0.1}O_2$ microspheres.

indicate that the Ni : Co : Mn molar ratio is approximately 8 : 1 : 1, displaying quite good consistency with the stoichiometric ratio.

The low-magnification SEM image of the holistic precursor (Fig. 3a) shows a micro-spherical morphology with an average sphere diameter of 5 μm. The high-magnification SEM image of a single sphere (Fig. 3b) shows that numerous highly ordered $Ni_{0.8}Co_{0.1}Mn_{0.1}(OH)_2$ nanoflakes are crisscrossed and perpendicular to the surface of the $Ni_{0.8}Co_{0.1}Mn_{0.1}O_x$ microsphere, forming the well-organized flower-ball-like hierarchical precursor, $Ni_{0.8}Co_{0.1}Mn_{0.1}(OH)_2@Ni_{0.8}Co_{0.1}Mn_{0.1}O_x$. The TEM image in Fig. 3c confirms that the precursor particles maintain a regular spherical shape, and the abundant voids in the $Ni_{0.8}Co_{0.1}Mn_{0.1}O_x$ microspheres are covered with a compact hydroxide layer. It is evident from Fig. 3d that the precursor is composed of two heterogeneous phases. The core of the microsphere is characterized by numerous closely packed nanoparticles, whose features match those of the spray pyrolyzed $Ni_{0.8}Co_{0.1}Mn_{0.1}O_x$ microspheres well (Fig. S1, ESI†). Abundant $Ni_{0.8}Co_{0.1}Mn_{0.1}(OH)_2$ nanoflakes integrate onto the surface of the $Ni_{0.8}Co_{0.1}Mn_{0.1}O_x$

microspheres, forming a thick layer of about 0.8 μm. The SEM image of the $LiNi_{0.8}Co_{0.1}Mn_{0.1}O_2$ cathode (Fig. 3e) exhibits micro-sized spheres with good dispersity and uniformity. The micron-sized microspheres are composed of submicron-sized primary particles with clean surfaces, as shown in Fig. 3f. The particle size distribution of $Ni_{0.8}Co_{0.1}Mn_{0.1}O_x$, $Ni_{0.8}Co_{0.1}Mn_{0.1}(OH)_2@Ni_{0.8}Co_{0.1}Mn_{0.1}O_x$ and the two as-prepared cathodes (Fig. S2, ESI†) confirm that the $LiNi_{0.8}Co_{0.1}Mn_{0.1}O_2$ cathode prepared from $Ni_{0.8}Co_{0.1}Mn_{0.1}O_x$ comprises submicron-sized particles, while the $LiNi_{0.8}Co_{0.1}Mn_{0.1}O_2$ cathode prepared from $Ni_{0.8}Co_{0.1}Mn_{0.1}(OH)_2@Ni_{0.8}Co_{0.1}Mn_{0.1}O_x$ comprises micron-sized particles. The sample shows a uniform distribution of particle size and mainly exists as grains with diameters of 3–5 μm. The TEM image in Fig. 3g shows that the microspheres are solid or have small-sized hollow spaces, which is revealed by the consistent contrast in the center and perimeter of the microspheres.

1824 | Mater. Chem. Front., 2018, 2, 1822–1828

This journal is © The Royal Society of Chemistry and the Chinese Chemical Society 2018

The cross-sectional SEM in Fig. 3h further confirms the interior structure of the $LiNi_{0.8}Co_{0.1}Mn_{0.1}O_2$ cathode. Strikingly, the co-precipitated hydroxide layer could prevent the $Ni_{0.8}Co_{0.1}Mn_{0.1}O_x$ microspheres from fragmenting during the sintering process, yielding $LiNi_{0.8}Co_{0.1}Mn_{0.1}O_2$ spheres with a solid or small-sized hollow interior structure. As a result, the resultant $LiNi_{0.8}Co_{0.1}Mn_{0.1}O_2$ exhibits a higher tap density (1.57 to 1.91 g cm^{-3}) due to better flowability and lower specific area (2.37 to 0.78 g m^2 g^{-1}) compared to the sample prepared from the spray-pyrolyzed precursor.

In order to observe the integration process of co-precipitated $Ni_{0.8}Co_{0.1}Mn_{0.1}(OH)_2$ nanoflakes onto the $Ni_{0.8}Co_{0.1}Mn_{0.1}O_x$ microspheres, samples of the precursor were collected every 0.5 h during the co-precipitation reaction. Fig. 4 shows SEM images of the $Ni_{0.8}Co_{0.1}Mn_{0.1}(OH)_2@Ni_{0.8}Co_{0.1}Mn_{0.1}O_x$ precursor samples obtained at different time intervals. It can be observed that co-precipitated hydroxide nanoflakes integrate on the surface of the $Ni_{0.8}Co_{0.1}Mn_{0.1}O_x$ microspheres rather than nucleate alone in the solution (Fig. 4a and b). Note that the $Ni_{0.8}Co_{0.1}Mn_{0.1}(OH)_2$ nanosheets grow evenly on the surface of the $Ni_{0.8}Co_{0.1}Mn_{0.1}O_x$ microspheres without regional disparities after 1 h of the co-precipitation reaction (Fig. 4c and d).

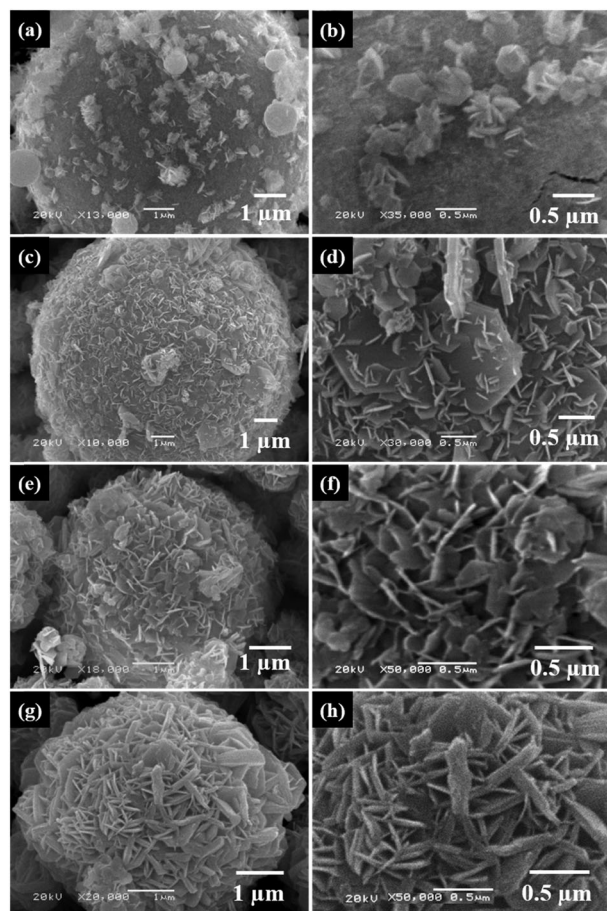Fig. 4 SEM of the $Ni_{0.8}Co_{0.1}Mn_{0.1}(OH)_2@Ni_{0.8}Co_{0.1}Mn_{0.1}O_x$ precursor obtained at different time intervals during the co-precipitation reaction: (a and b) 0.5 h; (c and d) 1 h; (e and f) 1.5 h; (g and h) 2 h.

Fig. 4e shows a uniform layer of $Ni_{0.8}Co_{0.1}Mn_{0.1}(OH)_2$ nanosheets integrated on the $Ni_{0.8}Co_{0.1}Mn_{0.1}O_x$ microspheres. The high-magnification image (Fig. 4f) reveals that numerous highly ordered $Ni_{0.8}Co_{0.1}Mn_{0.1}(OH)_2$ nanosheets are crisscrossed and perpendicular to the surface of the $Ni_{0.8}Co_{0.1}Mn_{0.1}O_x$ microspheres, and void spaces are present between adjacent nanosheets, forming the flower-ball-like hierarchical composite $Ni_{0.8}Co_{0.1}Mn_{0.1}(OH)_2@Ni_{0.8}Co_{0.1}Mn_{0.1}O_x$ precursor. As the co-precipitation reaction time is prolonged, the $Ni_{0.8}Co_{0.1}Mn_{0.1}(OH)_2$ nanosheets grow thicker and more compact, densely integrating onto the spray pyrolyzed $Ni_{0.8}Co_{0.1}Mn_{0.1}O_x$ microspheres (Fig. 4g and h). The well-organized $Ni_{0.8}Co_{0.1}Mn_{0.1}O_x@Ni_{0.8}Co_{0.1}Mn_{0.1}(OH)_2$ microspheres with diameters of greater than 3 μm were successfully produced. To further explain how the co-precipitated hydroxides prevent the $Ni_{0.8}Co_{0.1}Mn_{0.1}O_x$ microspheres from fragmenting during sintering, SEM images of $LiNi_{0.8}Co_{0.1}Mn_{0.1}O_2$ prepared from the precursor obtained at 1.5 and 2 h during the co-precipitation reaction were examined (Fig. S3, ESI†). After 1.5 h of the co-precipitation reaction, many of the precursor microspheres turn into submicron-sized particles after annealing. By comparison, the sample prepared from the precursor after 2 h of the co-precipitation reaction exhibits a micro-sized spherical shape with good dispersity and uniformity. The compact surface layer of the cathode microspheres is composed of many primary nanosheets, obtained from the co-precipitated $Ni_{0.8}Co_{0.1}Mn_{0.1}(OH)_2$ nanosheets after the lithiation reaction. Therefore, the highly ordered integrated $Ni_{0.8}Co_{0.1}Mn_{0.1}(OH)_2$ nanosheets can prevent the $Ni_{0.8}Co_{0.1}Mn_{0.1}O_x$ microspheres from fragmenting during sintering. A thicker and more compact $Ni_{0.8}Co_{0.1}Mn_{0.1}(OH)_2$ nanosheet layer is more beneficial to attain cathodes with a regular spherical morphology.

Fig. 5a shows a comparison of the 1st CV curve of $LiNi_{0.8}Co_{0.1}Mn_{0.1}O_2$ cathodes prepared from spray pyrolyzed $Ni_{0.8}Co_{0.1}Mn_{0.1}O_x$ and $Ni_{0.8}Co_{0.1}Mn_{0.1}(OH)_2@Ni_{0.8}Co_{0.1}Mn_{0.1}O_x$, respectively. It shows a reduced gap between the oxidation and reduction peak of the phase transition from H1 to M.[44] Moreover, the relieved degrees of the phase transition from H2 to H3 for $LiNi_{0.8}Co_{0.1}Mn_{0.1}O_2$ prepared from $Ni_{0.8}Co_{0.1}Mn_{0.1}(OH)_2@Ni_{0.8}Co_{0.1}Mn_{0.1}O_x$ can also be observed. These results indicate that the sample prepared from $Ni_{0.8}Co_{0.1}Mn_{0.1}(OH)_2@Ni_{0.8}Co_{0.1}Mn_{0.1}O_x$ shows a lower degree of polarization and a better structure stability than that prepared from $Ni_{0.8}Co_{0.1}Mn_{0.1}O_x$.[44,45] The initial charge–discharge curves of both samples at 0.1C are shown in Fig. 5b. The large specific area of $LiNi_{0.8}Co_{0.1}Mn_{0.1}O_2$ prepared from $Ni_{0.8}Co_{0.1}Mn_{0.1}O_x$ increases the contact area between the cathode and electrolyte. As a result, it delivers a high initial charge capacity of 252 mA h g^{-1}. This indicates that more Li$^+$ ions de-intercalate from the cathode during the first charging, leading to the collapse of the crystal structure. Meanwhile, for the micron-sized $LiNi_{0.8}Co_{0.1}Mn_{0.1}O_2$ spheres with lower specific surface areas, the decreased contact area with the electrolyte ensures a moderate initial charge capacity (234 mA h g^{-1}). As such, the initial coulombic efficiency is improved from 79.9% to 85.3%. The cycle performance of $LiNi_{0.8}Co_{0.1}Mn_{0.1}O_2$ prepared from $Ni_{0.8}Co_{0.1}Mn_{0.1}(OH)_2@Ni_{0.8}Co_{0.1}Mn_{0.1}O_x$ is presented in Fig. 5c. After 300 cycles at a rate of

This journal is © The Royal Society of Chemistry and the Chinese Chemical Society 2018

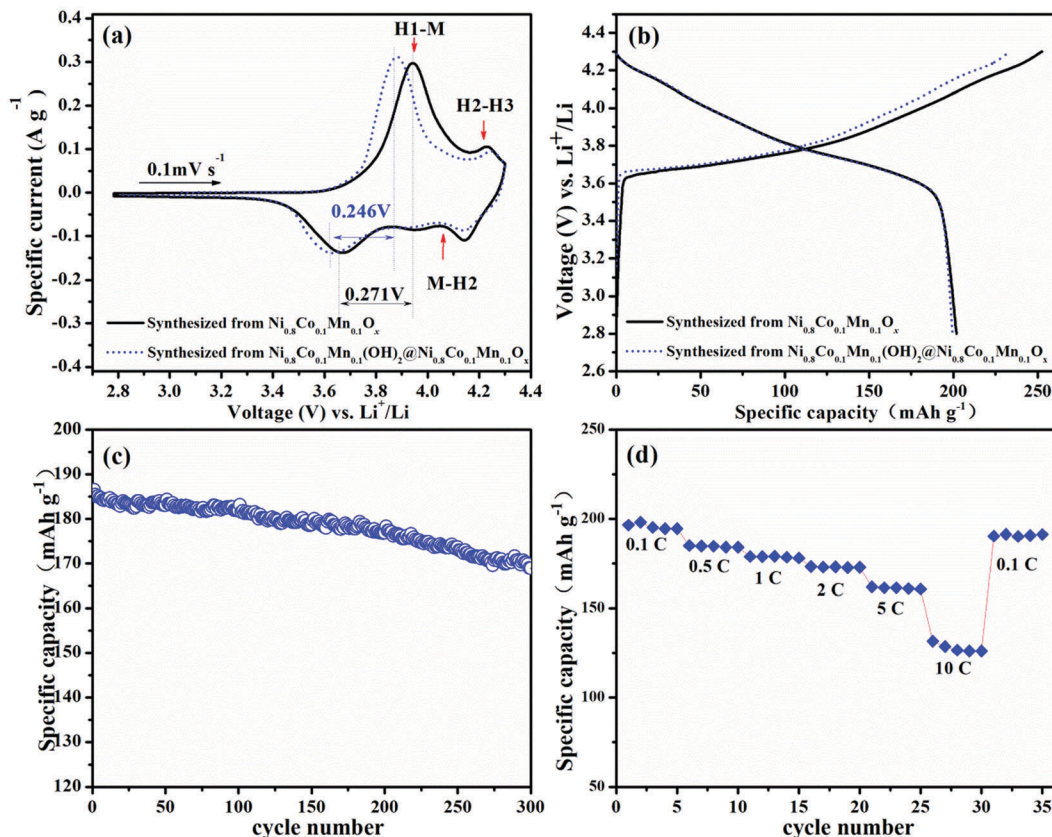Mater. Chem. Front., 2018, 2, 1822–1828 | 1825

Fig. 5 (a) CV curves (0.1 mV s^{-1}) and (b) initial charge−discharge profiles (0.28C) of LiNi$_{0.8}$Co$_{0.1}$Mn$_{0.1}$O$_2$ prepared from Ni$_{0.8}$Co$_{0.1}$Mn$_{0.1}$O$_x$ and Ni$_{0.8}$Co$_{0.1}$Mn$_{0.1}$(OH)$_2$@Ni$_{0.8}$Co$_{0.1}$Mn$_{0.1}$O$_x$. (c) Cycle performance of the LiNi$_{0.8}$Co$_{0.1}$Mn$_{0.1}$O$_2$ spheres at a rate of 1C. (d) Rate capability of the LiNi$_{0.8}$Co$_{0.1}$Mn$_{0.1}$O$_2$ spheres in the rate range of 0.1–10C.

1C, it delivers a discharge capacity of 169 mA h g^{-1} with a capacity retention of 90.5%. Table 1 shows the cycle performance of many previously reported LiNi$_{0.8}$Co$_{0.1}$Mn$_{0.1}$O$_2$ materials, including samples directly prepared *via* spray pyrolysis (Fig. S4, ESI†)[39] and co-precipitation (Fig. S5, ESI†),[46] demonstrating the excellent cycle stability of the cathode prepared from Ni$_{0.8}$Co$_{0.1}$Mn$_{0.1}$(OH)$_2$@Ni$_{0.8}$Co$_{0.1}$Mn$_{0.1}$O$_x$. The sample also shows superior rate capability and a reversible capacity of 128.6 mA h g^{-1} even at 10C (Fig. 5d). When the current density is back to 0.1C after high-rate testing, the capacity is able to recover well (191 mA h g^{-1}).

Fig. 6 shows the EIS of LiNi$_{0.8}$Co$_{0.1}$Mn$_{0.1}$O$_2$ prepared from Ni$_{0.8}$Co$_{0.1}$Mn$_{0.1}$O$_x$ and Ni$_{0.8}$Co$_{0.1}$Mn$_{0.1}$(OH)$_2$@Ni$_{0.8}$Co$_{0.1}$Mn$_{0.1}$O$_x$ after different cycles. The Nyquist plots are composed of two semicircles and a slope line in the charge state. One semicircle in the high frequency zone can be attributed to the SEI film resistance R_{sf}, the other semicircle in the medium frequency zone represents the charge-transfer resistance R_{ct}, and the slope line in the low frequency region is equivalent to the Warburg impedance Z_w. The EIS fitting results of the two samples are listed in Table 2. For the sample prepared from Ni$_{0.8}$Co$_{0.1}$Mn$_{0.1}$(OH)$_2$@Ni$_{0.8}$Co$_{0.1}$Mn$_{0.1}$O$_x$, the SEI film resistance R_{sf} increases

Table 1 Comparisons of cycling performances of the as-prepared LiNi$_{0.8}$Co$_{0.1}$Mn$_{0.1}$O$_2$ cathode in this work and previously reported LiNi$_{0.8}$Co$_{0.1}$Mn$_{0.1}$O$_2$ cathodes

Synthetic method of the precursor	Modifications	Cycle number	Current density	Remaining discharge capacity (mA h g^{-1})	Capacity retention (%)	Ref.
Co-precipitation	Pristine	100	0.2C	169	94.8	47
Co-precipitation	Fluorine doped	100	1C	160	94.3	48
Co-precipitation	Concentration graded	100	1C	173	93.2	49
Sol–gel	Li$_3$PO$_4$ and PPy coated	50	0.1C	—	95.1	50
Sol–gel	Pristine	100	0.5C	—	75.8	51
Co-precipitation	Pristine	100	0.5C	—	73.8	
Atomization co-precipitation	Pristine	100	1C	153	89.6	52
Spray pyrolysis	Pristine	100	1C	173	95.6	39
Co-precipitation	Pristine	100	1C	164	91.2	46
Spray pyrolysis with co-precipitation	Pristine	100	1C	173	97.5	This work
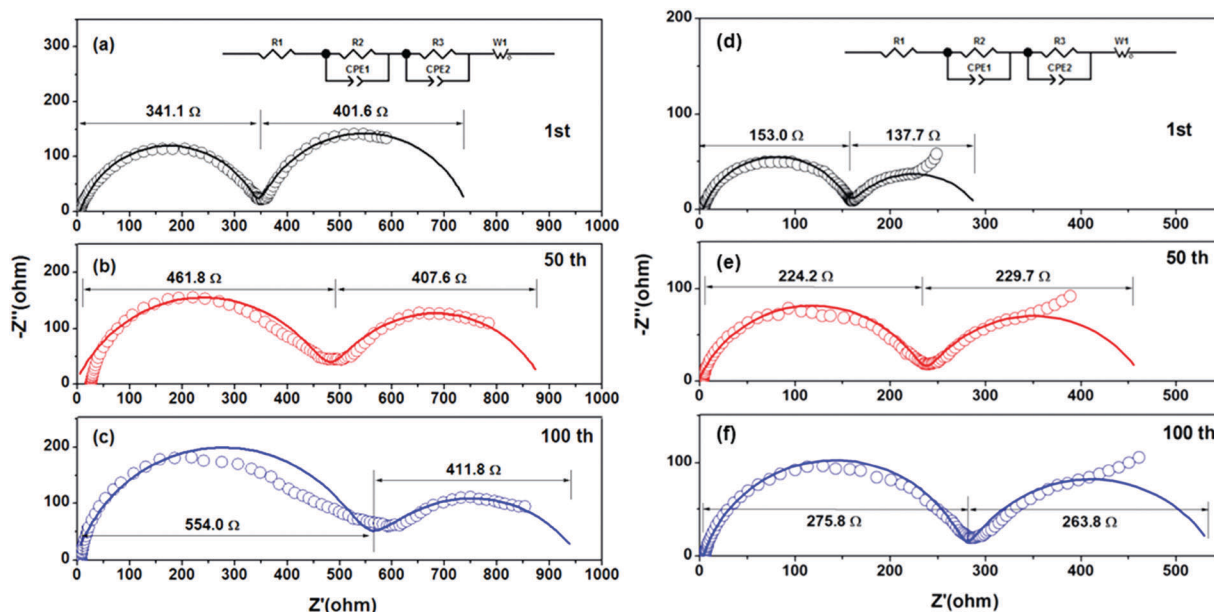
Fig. 6 EIS of $LiNi_{0.8}Co_{0.1}Mn_{0.1}O_2$ prepared from (a–c) $Ni_{0.8}Co_{0.1}Mn_{0.1}O_x$ and from (d–f) $Ni_{0.8}Co_{0.1}Mn_{0.1}(OH)_2@Ni_{0.8}Co_{0.1}Mn_{0.1}O_x$ after different cycles: (a and d) 1st; (b and e) 50th; (c and f) 100th.

Table 2 EIS fitting results of the submicron $LiNi_{0.8}Co_{0.1}Mn_{0.1}O_2$ sample prepared from $Ni_{0.8}Co_{0.1}Mn_{0.1}O_x$ and the $LiNi_{0.8}Co_{0.1}Mn_{0.1}O_2$ microsphere sample prepared from $Ni_{0.8}Co_{0.1}Mn_{0.1}(OH)_2@Ni_{0.8}Co_{0.1}Mn_{0.1}O_x$ after different cycles

	Submicron $LiNi_{0.8}Co_{0.1}Mn_{0.1}O_2$ particles			$LiNi_{0.8}Co_{0.1}Mn_{0.1}O_2$ microspheres		
Sample	1st	50th	100th	1st	50th	100th
R_{sf} (Ω)	341.1	461.8	554.0	153.0	224.2	275.8
R_{ct} (Ω)	401.6	407.6	411.8	137.7	229.7	263.8

slightly as the cycling number increases, indicating that the SEI on the surface of the electrode thickened slightly. The charge transfer impedance, R_{ct}, increased slightly in the first 50 cycles (from 137.7 Ω to 229.7 Ω), while almost remaining unchanged in the subsequent 50 cycles (from 229.7 Ω to 263.8 Ω), indicating that a stable interface is formed between the electrode and the electrolyte. The fragmented submicron $LiNi_{0.8}Co_{0.1}Mn_{0.1}O_2$ particles prepared from the spray pyrolyzed $Ni_{0.8}Co_{0.1}Mn_{0.1}O_x$ microspheres have a higher R_{sf} resistance compared with the $LiNi_{0.8}Co_{0.1}Mn_{0.1}O_2$ microspheres due to more interface resistance caused by the higher surface area. This further validates the above-mentioned reasons for the improved electrochemical properties of the $LiNi_{0.8}Co_{0.1}Mn_{0.1}O_2$ spheres.

4. Conclusions

In summary, a novel hierarchical architecture of $Ni_{0.8}Co_{0.1}Mn_{0.1}(OH)_2@Ni_{0.8}Co_{0.1}Mn_{0.1}O_x$ has been firstly constructed *via* spray pyrolysis followed by a co-precipitation method. The co-precipitated hydroxides could prevent the $Ni_{0.8}Co_{0.1}Mn_{0.1}O_x$ microspheres from fragmenting during sintering, thus yielding $LiNi_{0.8}Co_{0.1}Mn_{0.1}O_2$ spheres with a hollow interior morphology.

The as-prepared $LiNi_{0.8}Co_{0.1}Mn_{0.1}O_2$ spheres exhibited improved tap density, enhanced cycle performance and superior rate capability compared to $LiNi_{0.8}Co_{0.1}Mn_{0.1}O_2$ prepared from spray pyrolyzed $Ni_{0.8}Co_{0.1}Mn_{0.1}O_x$. This work provides a promising route to design hierarchical architectures for electrode materials.

Conflicts of interest

There are no conflicts to declare.

Acknowledgements

References

1 G. Liu, *Renewable Sustainable Energy Rev.*, 2014, **31**, 611–621.
2 Q. Deng, C. Lu and C. Yu, *Indoor Built Environ.*, 2015, **24**, 324–339.
3 J. Lan, K. Wang, Q. Yuan and X. Wang, *Mater. Chem. Front.*, 2017, **1**, 1217–1222.
4 X. Yan, Y. Liu, J. Lan, Y. Yu, J. Murowchick, X. Yang and Z. Peng, *Mater. Chem. Front.*, 2018, **2**, 96–101.
5 J. Wang, H. Tang, H. Wang, R. Yu and D. Wang, *Mater. Chem. Front.*, 2017, **1**, 414–430.

This journal is © The Royal Society of Chemistry and the Chinese Chemical Society 2018

Mater. Chem. Front., 2018, **2**, 1822–1828 | **1827**

6 J. Wang, H. Tang, H. Ren, R. Yu, J. Qi, D. Mao, H. Zhao and D. Wang, *Adv. Sci.*, 2014, **1**, 1719–1720.

7 Q. Bao, Y. Chong, Y. Xia and Z. Liu, *ACS Appl. Mater. Interfaces*, 2017, **9**, 3661–3666.

8 C. Yan, W. Xi, W. Si, J. Deng and O. G. Schmidt, *Adv. Mater.*, 2013, **25**, 644.

9 H. Hou, C. E. Banks, M. Jing, Y. Zhang and X. Ji, *Adv. Mater.*, 2015, **27**, 7861–7866.

10 X. Feng, M. Ouyang, X. Liu, L. Lu, Y. Xia and X. He, *Energy Storage Mater.*, 2017, **10**, 246–267.

11 J. Wang, G. Zhang, Z. Liu, H. Li, Y. Liu, Z. Wang, X. Li, K. Shih and L. Mai, *Nano Energy*, 2018, **44**, 272–278.

12 Y. Zhou, H. Guo, G. Yan, Z. Wang, X. Li, Z. Yang, A. Zheng and J. Wang, *Chem. Commun.*, 2018, **54**, 3755–3758.

13 J. Wang, N. Yang, H. Tang, Z. Dong, Q. Jin, M. Yang, D. Kisailus, H. Zhao, Z. Tang and D. Wang, *Angew. Chem., Int. Ed.*, 2013, **52**, 6417–6420.

14 H. Tian, H. Liu, T. Yang, J. P. Veder, G. Wang, M. Hu, S. Wang, M. Jaroniec and J. Liu, *Mater. Chem. Front.*, 2017, 823–830.

15 G. K. Min, M. Jo, Y. S. Hong and J. Cho, *Chem. Commun.*, 2009, 218–220.

16 Y. Zhou, H. Guo, Y. Yong, Z. Wang, X. Li and R. Zhou, *Mater. Lett.*, 2017, **195**, 164–167.

17 H. Meng, X. Pang and Z. Zhen, *J. Power Sources*, 2013, **237**, 229–242.

18 L. F. Chen, Y. Lu, L. Yu and X. W. Lou, *Energy Environ. Sci.*, 2017, **10**, 1777–1783.

19 X. Yao, L. Deng, C. Wang, L. Peng, P. Gang, Y. S. Hu, L. Hong, L. Chen and X. Xu, *Nano Lett.*, 2016, **16**, 7148–7154.

20 W. Li, Y. Tang, W. Kang, Z. Zhang, X. Yang, Y. Zhu, W. Zhang and C.-S. Lee, *Small*, 2015, **11**, 1345–1351.

21 S. Xu, C. M. Hessel, H. Ren, R. Yu, Q. Jin, M. Yang, H. Zhao and D. Wang, *Energy Environ. Sci.*, 2014, **7**, 632–637.

22 W. Pan, W. Peng, G. Yan, H. Guo, Z. Wang, X. Li, W. Gui, J. Wang and N. Chen, *Energy Technol.*, 2018, DOI: 10.1002/ente.201800253.

23 H. Ren, R. Yu, J. Wang, Q. Jin, M. Yang, D. Mao, D. Kisailus, H. Zhao and D. Wang, *Nano Lett.*, 2014, **14**, 6679–6684.

24 P. Huang, J. Liu, F. Wei, Y. Zhu, X. Wang, C. Cao and W. Song, *Mater. Chem. Front.*, 2017, **1**, 1550–1555.

25 W. Liu, P. Oh, X. Liu, M. J. Lee, W. Cho, S. Chae, Y. Kim and J. Cho, *Angew. Chem., Int. Ed.*, 2015, **54**, 4440–4457.

26 Y. Ding, D. Mu, B. Wu, R. Wang, Z. Zhao and F. Wu, *Appl. Energy*, 2017, **195**, 586–599.

27 A. Manthiram, B. Song and W. Li, *Energy Storage Mater.*, 2016, **6**, 125–139.

28 G. L. Messing, S. C. Zhang and G. V. Jayanthi, *J. Am. Ceram. Soc.*, 1993, **76**, 2707–2726.

29 J. Leng, Z. Wang, X. Li, H. Guo, H. Li, K. Shih, G. Yan and J. Wang, *J. Mater. Chem. A*, 2017, **5**, 14996–15001.

30 T. Li, J. Wang, Z. Wang, H. Guo, Y. Li and X. Li, *J. Mater. Chem. A*, 2017, **5**, 13469–13474.

31 D. Guan, Q. Yu, C. Xu, C. Tang, L. Zhou, D. Zhao and L. Mai, *Nano Res.*, 2017, 1–9.

32 H. C. Wu, Z. Z. Guo, M. H. Yang, C. H. Lu, T. Y. Wu and I. Taniguchi, *Chem. Lett.*, 2005, **34**, 1398–1399.

33 L. Zhang, K. Takada, N. Ohta, K. Fukuda and T. Sasaki, *J. Power Sources*, 2005, **146**, 598–601.

34 T. N. L. Doan and I. Taniguchi, *J. Power Sources*, 2011, **196**, 1399–1408.

35 M. Konarova and I. Taniguchi, *J. Power Sources*, 2009, **194**, 1029–1035.

36 J. Liu, T. E. Conry, X. Song, L. Yang, M. M. Doeff and T. J. Richardson, *J. Mater. Chem. A*, 2011, **21**, 9984–9987.

37 K. Matsuda and I. Taniguchi, *Kagaku Kogaku Ronbunshu*, 2003, **29**, 232–237.

38 I. Taniguchi, C. K. Lim, D. Song and M. Wakihara, *Solid State Ionics*, 2002, **146**, 239–247.

39 T. Li, X. Li, Z. Wang and H. Guo, *J. Power Sources*, 2017, **342**, 495–503.

40 M. Lengyel, D. Elhassid, G. Atlas, W. T. Moller and R. L. Axelbaum, *J. Power Sources*, 2014, **266**, 175–178.

41 S. H. Ju and Y. C. Kang, *J. Power Sources*, 2008, **178**, 387–392.

42 S. H. Ju, H. C. Jang and Y. C. Kang, *Electrochim. Acta*, 2007, **52**, 7286–7292.

43 T. Li, X. Li, Z. Wang, H. Guo, W. Peng and K. Zeng, *Mater. Lett.*, 2015, **159**, 39–42.

44 J. Yang and Y. Y. Xia, *ACS Appl. Mater. Interfaces*, 2016, **8**, 1297–1308.

45 H. H. Sun, W. Choi, J. K. Lee, I. H. Oh and H. G. Jung, *J. Power Sources*, 2015, **275**, 877–883.

46 K. Meng, Z. Wang, H. Guo, X. Li and J. Wang, *Hydrometallurgy*, 2017, **174**C, 1–9.

47 S. Zhong, M. Lai, W. Yao and Z. Li, *Electrochim. Acta*, 2016, **212**, 343–351.

48 Y. Peng, Z. Wang, H. Guo, X. Xiong and X. Li, *Electrochim. Acta*, 2013, **92**, 1–8.

49 C. Hua, K. Du, C. Tan, Z. Peng, Y. Cao and G. Hu, *J. Alloys Compd.*, 2014, **614**, 264–270.

50 S. Chen, T. He, Y. Su, Y. Lu, L. Bao, L. Chen, Q. Zhang, J. Wang, R. Chen and F. Wu, ACS Appl. Mater. Interfaces, 2017.

51 H. Lu, H. Zhou, A. M. Svensson, A. Fossdal, E. Sheridan, S. Lu and F. Vullum-Bruer, *Solid State Ionics*, 2013, **s249–250**, 105–111.

52 X. Zheng, X. Li, B. Zhang, Z. Wang, H. Guo, Z. Huang, G. Yan, D. Wang and Y. Xu, *Ceram. Int.*, 2016, **42**, 644–649.

1828 | *Mater. Chem. Front.*, 2018, **2**, 1822–1828

This journal is © The Royal Society of Chemistry and the Chinese Chemical Society 2018